Journal of
Materials Chemistry A

ROYAL SOCIETY
OF CHEMISTRY

PAPER

View Article Online
View Journal | View Issue

Check for updates

Cite this: *J. Mater. Chem. A*, 2023, **11**, 17272

High performance N-doped carbon nanosheet/MnO_2 cathode derived from bacterial cellulose for aqueous Zn-ion batteries†

Wenhai Wang,[ab] Ashley P. Black,[b] Cheng Liu,[b] Vlad Martin-Diaconescu,[c]
Laura Simonelli[c] and Dino Tonti*[b]

Received 10th March 2023
Accepted 27th July 2023

DOI: 10.1039/d3ta01487h

rsc.li/materials-a

Rechargeable aqueous Zn-ion batteries (ZIBs) have obtained extensive attention owing to their high safety, low-cost, environmental friendliness and high energy density. Nevertheless, developing suitable cathode materials remains challenging due to requirements for appropriate microstructure. We present a porous N-doped carbon nanosheet/MnO_2 (NCS/MnO_2) derived from bacterial cellulose (BC) by a simple route. BC chunks were soaked in urea solution and then carbonized under Ar flow at 900 °C. N-doped carbon nanosheets were obtained and MnO_2 was added by reaction with $NaMnO_4$. Benefiting from both the conductivity and porosity of the NCS support, the NCS/MnO_2 composite delivers a high capacity and long cycling stability (114 mA h g^{-1} at 2 A g^{-1} after 1800 cycles). The electrode reaction mechanism was further investigated and the MnO_2 dissolution/deposition mechanism was confirmed, with a critical role of zinc sulfate hydroxide (ZSH) to assist the deposition of MnO_2.

Introduction

Due to the limited amount of fossil energy and the climate problems, the demand to explore renewable energy systems becomes more urgent. To favor their exploitation enormous efforts have been devoted to developing suitable energy storage systems. Li-ion batteries are considered as one of the most convincing commercial options, however the safety problems related to organic electrolyte and limited lithium abundance restrict their development for large-scale application.[1] Recently, rechargeable aqueous zinc-ion batteries (ZIBs) with nearly neutral electrolytes have obtained enormous interest.[2,3] Indeed, metal zinc possesses a striking theoretical capacity (820 mA h g^{-1}), low reduction potential (−0.76 *vs.* SHE), excellent stability in water and large abundance.[4] Moreover, aqueous electrolytes are safer and cheaper than organic electrolyte,[5] and present much higher ionic conductivity.[6]

Despite aqueous ZIBs present important advantages, there are still many challenges for developing satisfactory cathodes. Various cathode materials (such as manganese-based oxides, Prussian blue analogues, vanadium based oxides and organic electrodes) have been explored for aqueous ZIBs.[7,8] Among them, MnO_2 has gained much interest, because of considerable capacity, decent voltage, low-cost and rich abundance.[9–11] However, MnO_2 exhibits poor electrical conductivity, seriously undermining the electrochemical performance of ZIBs.[12,13] To handle this problem, conductive polymers and carbon materials (graphene, CNT, N-doped carbon) have been integrated with MnO_2.[14–17] However, conductive polymers tend to degrade by swelling and shrink during cycling, which negatively affects the lifetime.[18,19] Instead, CNT and graphene are relatively high-cost, which restricts their commercial applications. N-doped carbon has emerged as an effective candidate thanks to lower cost, good electrical conductivity and good electrochemical properties.[20] In many reports, metal–organic frameworks (MOFs) were utilized as the sources of N-doped carbon.[17,21–23] Nevertheless MOFs are often difficult to prepare at a large-scale, and suffer poor chemical stability.[24–26] It is more appealing to fabricate N-doped carbons from biomass, which is usually facile, low-cost, ecofriendly and easy to scale up. Bacterial cellulose (BC) as a novel biomass material, typically produced from *Acetobacter xylinum*,[27,28] owns outstanding characteristics of purity, 3D porous structure and high water-absorbing capacity,[29–31] which make it employed in many fields such as food packing, biomedical field, water treatment, electrochemical energy storage and conversion.[32–34] BC has been exploited to develop N-doped carbons, by polymerization of polypyrrole, polyaniline, polyacrylonitrile on BC[35–37] or high temperature ammonia treatment[38] to introduce the nitrogen source. These ways are time-consuming, complicated or risky, thus their economic viability remains limited.

---

[a] Institute of Clean Energy and Advanced Nanocatalysis (iClean), School of Chemistry and Chemical Engineering, Anhui University of Technology, Maanshan 243002, China

[b] Institut de Ciència de Materials de Barcelona, Consejo Superior de Investigaciones Científicas (ICMAB-CSIC), Campus UAB Bellaterra, Barcelona, Spain. E-mail: dino.t@csic.es

[c] ALBA Synchrotron Light Source, 08290 Cerdanyola del Vallès, Barcelona, Spain

† Electronic supplementary information (ESI) available. See DOI: https://doi.org/10.1039/d3ta01487h

Here we report a simple, green and scalable fabrication of porous N-doped carbon/MnO_2 derived from BC, which is used as the cathode for ZIBs. In this process, BC was soaked in a urea solution to obtain the nitrogen source and then after carbonization porous N-doped carbon with an unexpected nanosheet morphology (NCS) was obtained. The MnO_2 deposition was achieved by a reaction between NCS and $NaMnO_4$. The ability of BC to acquire the nitrogen source by absorbing urea solution avoids more complex or hazardous routes. Meanwhile, the decomposition of absorbed urea on BC can create high porosity for NCS during the process of pyrolysis. Due to the resulting good conductive and high porosity NCS carbon, the resulting NCS/MnO_2 composite derived from BC shows a large capacity and long-term cyclability (114 mA h g^{-1} at 2 A g^{-1} after 1800 cycles). Furthermore, the electrochemical mechanism of NCS/MnO_2 is further scrutinized by multiple analytical methods. These results indicate that the mechanism of NCS/MnO_2 involves MnO_2 dissolution/deposition.

Experimental section

Materials

Bacterial cellulose (BC, Q-Phil Products International), urea (CH_4N_2O, Thermo Scientific), sodium permanganate solution ($NaMnO_4$, 40 wt% in H_2O, Sigma-Aldrich), commercial manganese dioxide (MnO_2, Sigma-Aldrich), zinc sulfate heptahydrate ($ZnSO_4\cdot7H_2O$, Labkem), manganese sulfate monohydrate ($MnSO_4\cdot H_2O$, Labkem), 1-methyl-2-pyrrolidone (C_5H_9NO, Sigma-Aldrich), polyvinylidene fluoride (PVDF, Sigma-Aldrich), carbon black (Super P, Timcal), carbon paper (Freudenberg, H2315, 210 μm thickness), Zn foil (Advent Research Materials Ltd, 0.125 mm thickness), glass fibre filter (PRAT DUMAS, 270 μm thickness).

Preparation of materials

Bacterial cellulose cubes (approx. size 15 × 15 × 15 mm^3) was purified by washing in Milli-Q water as described previously.[39,40] Then individual BC cubes were pressed by a ~150 g Teflon cylinder for 10 minutes to remove most water. The pressed BC was soaked in urea solution (0.1 g mL^{-1}) with stirring for 2 h. Then the soaked BC was extracted and dried in oven at 60 °C for 24 h. The dried BC was carbonized in a tubular furnace under an Ar flow of 100 mL min^{-1} with a ramp of 10 °C min^{-1} to 900 °C and kept there for 1 h.

N-doped carbon/MnO_2 preparation: 24 mg N-doped carbon was added in 35 mL solution containing 0.28 g $NaMnO_4$ and stirred for 4 h at room temperature. Then the product was washed by Milli-Q water for several times and dried at 60 °C for 24 h. Note that in spite of the large $NaMnO_4$ excess, according to thermogravimetric analysis MnO_2 is ~42% of the composite mass (see Results and discussion), which strongly suggests that in our conditions the reaction between $NaMnO_4$ and NCS is self-limited.

Carbon-w was produced from simply carbonizing purified BC in Ar atmosphere at 900 °C for 1 h, as in our previous article.[39] C/MnO_2 is then obtained by reaction between carbon-w and $NaMnO_4$, as described for N-doped carbon/MnO_2.

Characterization

FEI Quanta 200 FEG-ESEM equipment (15 kV voltage) was performed to obtain Scanning Electron Microscopy (SEM) images. JEOL JEM1210 TEM (voltage 120 kV) and JEM-2011 TEM (voltage 200 kV) were carried out to obtain Transmission electron microscopy (TEM) images. Scanning transmission electron microscopy was performed at a Tecnai G^2 F20 at 200 kV. Fourier transform infrared (FTIR) spectra of samples were conducted by a Jasco 4700 Spectrophotometer. Siemens D-5000 diffractometer with Cu Kα radiation was used to collect X-ray diffraction (XRD) patterns. Raman spectra of samples were recorded by a Renishaw InVia Raman Microscope with 633 nm laser. Thermogravimetric analysis (TGA) was done by a NETZSCH STA 449 F1 Jupiter equipment under air atmosphere with 10 °C min^{-1}. N_2 adsorption/desorption measurements were probed by Micromeritics ASAP 2020 equipment. X-Ray Photoelectron Spectroscopy (XPS) measurements were taken by a SPECS EA10P hemispherical analyzer with a monochromatic Al Kα source. The X-ray Absorption Spectroscopy (XAS) data were obtained at the Mn and Zn K-edges at the CLAESS beamline of the ALBA synchrotron light source.[41] The XAS spectra have been acquired in transmission mode by means of ionization chambers. The Si (111) double crystal monochromator was employed and the higher harmonic were rejected by appropriately choosing the incident angle and coating of the collimating and focusing mirror. The beam size was around 1 × 1 mm^2 with a total incoming flux around 10^{13} photons per s. The radiation damage was suppressed by an approximately 90% attenuation of the incoming beam using Al filters. *In situ* measurements were performed using modified coin cells with a 6 mm diameter Kapton windows and a 0.5 M $ZnSO_4$ with 0.05 M $MnSO_4$ aqueous electrolyte.

Electrochemical performance

To prepare cathodes, MnO_2 based materials, Super P and PVDF were mixed at a weight ratio of 7 : 2 : 1 in 1-methyl-2-pyrrolidone. Then the slurry was coated on a carbon paper and was dried in the oven (60 °C) for 24 h. The total loading on the carbon paper is *ca.* 1.0 mg cm^{-2}. The capacity is calculated by the mass of MnO_2 based materials. The Zn ion battery electrochemical performance of cathode materials were studied in Swagelok cells. The cells were assembled with Zn foil as the anode, glass fibre filter as the separator, 2 M $ZnSO_4$ with 0.2 M $MnSO_4$ aqueous electrolyte, and MnO_2 based materials as the cathode. The cyclic voltammetry measurements (CV) and electrochemical impedance spectroscopy (EIS, frequency range from 100 kHz to 100 mHz and an AC amplitude of 5 mV) measurements were performed by a Bio-logic VMP3 multichannel potentiostat. Galvanostatic discharge/charge tests were conducted by a battery cycling equipment (LANHE M340A).

Results and discussion

N-doped carbon was synthesized from the carbonization of urea-soaked BC and carbon-w was prepared from the pyrolysis of pure BC without urea. The morphologies and structure of prepared samples were compared by scanning electron microscopy (SEM) and transmission electron microscopy (TEM). N-doped carbon displays nanosheet structure and high porosity (Fig. 1a and d), and is labeled as NCS. In comparison, carbon-w shows more compact structure (Fig. S1a and c†), implying that urea works as a porogen for carbon. After NCS and carbon-w reacted with $NaMnO_4$, their morphologies barely changed (Fig. 1a–c, S1a and b†). TEM images further reveal some nanorods on NCS (Fig. 1d–f) and the corresponding selected area electron diffraction (SAED) depicts rings corresponding to interlayer distances of 0.24 and 0.21 nm (Fig. S2a†), corresponding to (006) and (−112) planes of MnO_2.[42,43] The energy-dispersive spectroscopy (EDS) elemental line profiles of NCS/MnO_2 confirm the existence of the elements of Mn and O for the nanorod (Fig. S2b†). At larger scale, EDS mapping images show that the elements C, N, Mn and O distribute uniformly in NCS/MnO_2 (Fig. 1g). The morphology of commercial MnO_2 instead is dominated by large irregular particles of several tens of micrometers along with smaller particles of less than one micrometer (Fig. S1a–f†).

X-ray diffraction (XRD) measurement was carried out to investigate the phase structures of NCS, carbon-w, C/MnO_2 and NCS/MnO_2. As shown Fig. 2a, carbon-w and NCS show a broad peak at around 26°, referring to the plane (002) of graphite carbon.[44,45] Both C/MnO_2 and NCS/MnO_2 exhibit a weak and broad peak at 36°, which can be indexed to the plane (006) of MnO_2.[46] X-ray absorption spectroscopy (XAS) reveals that the energy position of Mn peak for NCS/MnO_2 is close to reference MnO_2, further confirming the formation of MnO_2 on NCS (Fig. S3a†). Commercial MnO_2 was also investigated by XAS and XRD (Fig. S3†). Raman spectrum was used to quantify the graphitization degrees of carbon-w and NCS. There are in both samples two peaks located at 1350 cm^{-1} (D band) and 1600 cm^{-1} (G band), representing disordered and graphitized carbon (Fig. 2b).[47,48] The intensity ratio G to D band (I_D/I_G) is used to evaluate the degree of graphitization. The value of I_D/I_G for NCS is 1.12, which is lower than carbon-w (1.21). It implies that a higher graphitization can be obtained in the presence of urea, which is expected to infer better electron conduction.[49] After reacting with $NaMnO_4$, a new peak appearing at 640 cm^{-1} can be associated with the Mn-O stretching vibration of MnO_6 groups,[50] demonstrating the formation of MnO_2 both on carbon-w and NCS. Compared with carbon-w and NCS, the ratios of I_D/I_G for NCS/MnO_2 (1.18) and C/MnO_2 (1.27) increase. This indicates that the introduction of MnO_2 causes more defects into carbon-w and NCS, leading to more defective graphitic structures and lower degree of graphitization.[51,52]

The porous structure of NCS was inspected by N_2 adsorption–desorption measurement (Fig. S4a and Table S1†). Although the surface area of NCS (431 $m^2\ g^{-1}$) is lower than that of carbon-w (1009 $m^2\ g^{-1}$), its pore volume is much larger (0.86 *vs.* 0.19 $cm^3\ g^{-1}$). The pore size distribution curves show that the

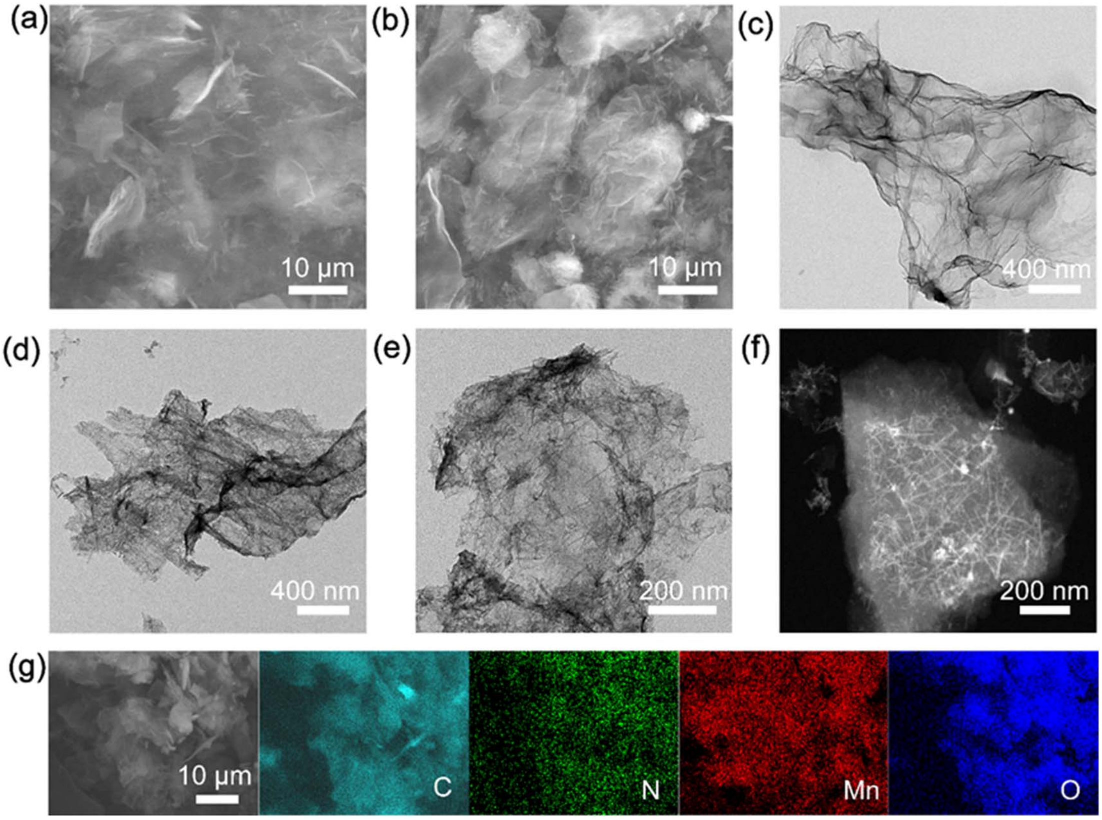

Fig. 1 Electron microscopy of prepared materials: SEM images of (a) NCS; (b) NCS/MnO_2. TEM images of (c) NCS; (d and e) NCS/MnO_2. (f) Scanning TEM of NCS/MnO_2. (g) Element mapping images of NCS/MnO_2.

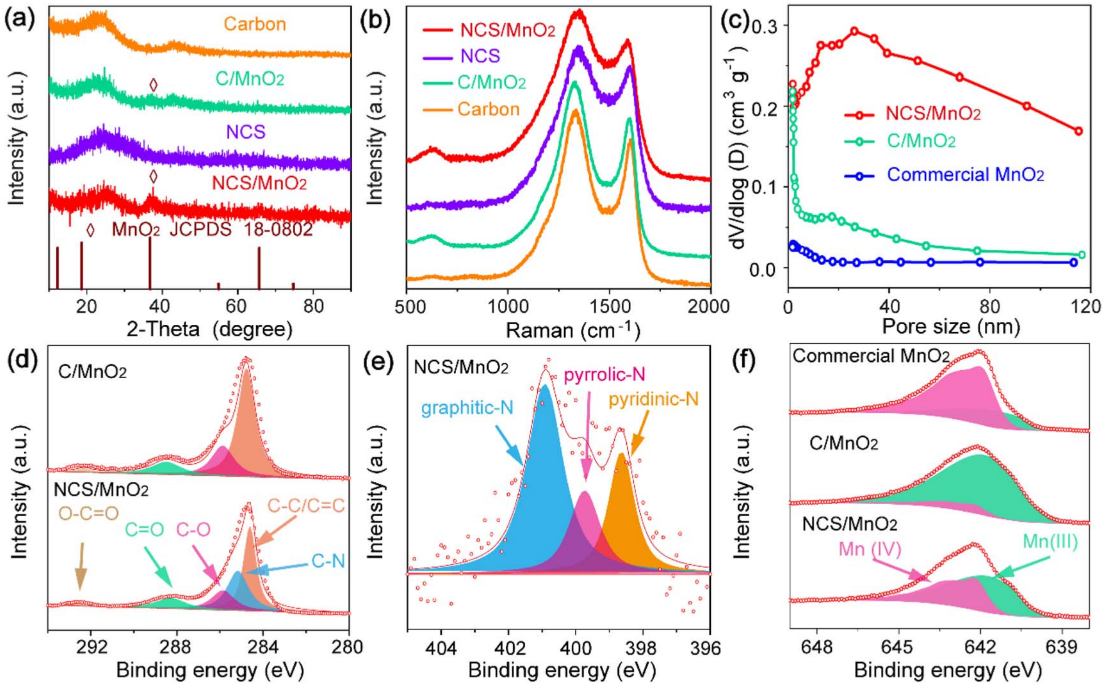

Fig. 2 Structural and surface characterization: (a) XRD patterns. (b) Raman spectra. (c) Pore size distribution. XPS spectra (d) C 1s, (e) N 1s, (f) Mn $2p_{3/2}$.

pore structure of NCS is predominately composed by mesopores and macropores (Fig. S4b†), leading to a high surface external area, while the pore structure of carbon-w mainly consists of micropores.[39] The high porosity of NCS can be attributed to the released ammonia and carbon dioxide gas from urea during cellulose carbonization.[53,54] After MnO_2 deposition, the surface area and pore volume of both carbons decrease (Table S1†). This is probably because some parts of NCS and carbon-w were consumed and the introduction of MnO_2 blocked pores to some extent, resulting in decreased surface areas and pore volumes, although after MnO_2 depositions trends are similar to those found with carbon substrates. Despite NCS/MnO_2 does not have a larger surface area (229 m^2 g^{-1}) than C/MnO_2 (401 m^2 g^{-1}), NCS/MnO_2 exhibits a larger pore volume (0.42 cm^3 g^{-1}) than C/MnO_2 (0.12 cm^3 g^{-1}). In addition, the porous structure of NCS/MnO_2 mainly consists of mesopores and macropores, while the pore structures of C/MnO_2 and commercial MnO_2 are dominated by micropores (Fig. 2c). These results demonstrate that NCS/MnO_2 possesses higher porosity than C/MnO_2 and commercial MnO_2. Electrodes of high porosity is more favorable for fast ion transfer, which can shorten the diffusion path.[55,56] This has effect also on the content of MnO_2 in NCS/MnO_2, revealed by thermogravimetric analysis (TGA), which is about 42% (Fig. S5†), much higher than in C/MnO_2, about 11%. The high porosity of NCS/MnO_2 favors the diffusion of $NaMnO_4$ into the bulk and the MnO_2 deposition can take place on the surface and inside of NCS at the same time.[57,58] In contrast, the diffusion path of $NaMnO_4$ into carbon-w with low porosity is difficult and the reaction between carbon-w and $NaMnO_4$ mainly occurs on the surface of carbon-w. As a consequence, the larger pore volume of NCS is better filled by MnO_2, resulting in much higher mass content of MnO_2 in NCS/MnO_2 than in C/MnO_2.

To detect the surface chemical composition and chemical state of these samples, X-ray photoelectron spectroscopy (XPS) was performed. N 1s peak is observed in the full spectrum of NCS (Fig. S6†), indicating that N was successfully doped into carbon. The nitrogen content of NCS is 4.8 at%. After NCS reacted with $NaMnO_4$, C 1s, N 1s, Mn 2p and O 1s peaks are obvious in the full spectrum of NCS/MnO_2 (Fig. S6†). The C 1s spectrum of NCS/MnO_2 can be fitted into 4 peaks at 284.6, 285.2, 285.9, 288.3 and 292.5 eV (Fig. 2d), corresponding to C–C/C=C, C–N, C–O, C=O and O–C=O.[59,60] The N 1s spectrum of NCS/MnO_2 can be divided into three peaks (Fig. 2e), attributed to pyridinic-N (398.6 eV), pyrrolic-N (399.7 eV) and graphitic-N (400.9 eV).[61] It has been shown that pyridinic-N and pyrrolic-N can enhance the electronic conductivity of carbon and hence promote the battery performance.[62,63] The binding energy of Mn 2p of C/MnO_2 and NCS/MnO_2 are similar to commercial MnO_2 (Fig. 2f and S7†), confirming the presence of Mn oxides in the prepared composites. Mn 2p peaks were deconvoluted into two multiplet components attributed to Mn^{3+} and Mn^{4+} according to the method proposed by Ilton *et al.*[64] The area of these peaks indicates significant Mn^{3+} fractions at the surface of these samples (Table S2†), particularly in the case of C/MnO_2. This could be attributed to the reductive environment provided by the carbon excess that supports the Mn oxides.

To evaluate the electrochemical performance of MnO_2 electrodes, full batteries with Zn foil anodes were assembled in Swagelok cells. As shown in Fig. 3a, cyclic voltammetry curve (CV) of all three cathodes tested present two pairs of reduction/

oxidation peaks, suggesting that they have similar redox reactions. But the currents of these peaks for NCS/MnO_2 are larger than C/MnO_2 and commercial MnO_2, demonstrating that NCS/MnO_2 possesses higher electrochemical activity and fast reaction kinetic.[65] The rate capabilities of cathodes were measured at different current densities (Fig. 3b). NCS/MnO_2 provides 226 mA h g^{-1} at 0.1 A g^{-1} (Fig. 3c). Even at high current densities of 1 A g^{-1}, NCS/MnO_2 still can deliver 210 mA h g^{-1}. C/MnO_2 and commercial MnO_2 were also measured as a comparison. C/MnO_2 and commercial MnO_2 demonstrate much lower capacities than NCS/MnO_2 at various current densities (Fig. 3b and S8†). In particular, the capacities of commercial MnO_2 (from 187 mA h g^{-1} at 0.1 A g^{-1} to 127 mA h g^{-1} at 1 A g^{-1}) and C/MnO_2 (from 77 mA h g^{-1} at 0.1 A g^{-1} to 53 mA h g^{-1} at 1 A g^{-1}) decrease greatly with the increment of the current density. The capacity at 1 A g^{-1} for commercial MnO_2 and C/MnO_2 are respectively 68% and 69% of that at 0.1 A g^{-1}, considerably lower than for NCS/MnO_2 (90%). The lower capacities compared to NCS/MnO_2 can be explained with the lower MnO_2 content of C/MnO_2 (as determined by TGA), and with the large number of coarse particles in the commercial MnO_2 sample. These results show that NCS/MnO_2 possesses an excellent rate performance.

To further evaluate the cycling stability, the electrodes were cycled at 0.2 A g^{-1} (Fig. 3d). The discharge capacities gradually increase during the cycling, which can be associated with an electrochemical activation process also reported by other authors on ZIB systems.[66] The capacity of NCS/MnO_2 increased to a larger extent than C/MnO_2 and commercial MnO_2, probably because of the high porosity of NCS/MnO_2, which can facilitate the deposition of MnO_2 during charge.[67] Among these electrodes, NCS/MnO_2 shows a higher capacity (358 mA h g^{-1}) than commercial MnO_2 (177 mA h g^{-1}) and C/MnO_2 (74 mA h g^{-1}) after 60 cycles. The NCS/MnO_2 capacity is even larger above 100 cycles (over 400 mA h g^{-1}, see Fig. S9†). The capacity of MnO_2-free NCS and carbon-w were also investigated (Fig. S10†). The capacities of NCS (60 mA h g^{-1}) and carbon-w (48 mA h g^{-1}) are similar at 0.2 A g^{-1} after 60 cycles. To evaluate the role of Mn^{2+} in the electrolyte, the Swagelok cell with NCS/MnO_2 as cathode was assembled without using $MnSO_4$ additive under the same conditions (Fig. S11†). The capacity of NCS/MnO_2 declines rapidly with cycle number. It is obvious that the addition of $MnSO_4$ can enhance the electrochemical reversibility. This confirms that the $MnSO_4$ additive can generate a proper equilibrium between Mn^{2+} dissolution and the re-oxidation of the Mn^{2+}, which improves the stability of the cathode.[68] In addition, the test without MnO_2 in the electrode demonstrates that capacity can even be provided by Mn^{2+} in the electrolyte, which precipitates as oxide during charge. However, the larger difference with the NCS sample shows the important contribution of MnO_2 already present inside the pores of the electrodes, which only the NCS texture allows to great extent.

The cycling stability of all electrodes were also investigated at a high current density of 2 A g^{-1}. There is a noticeable decay in capacity for NCS/MnO_2 (Fig. 3e) and the reason for attenuation was investigated. As shown in Fig. S12,† the 2nd discharge capacity (232 mA h g^{-1}) is lower than the 1st charge capacity (252 mA h g^{-1}). It demonstrates that less MnO_2 is dissolved on the 2nd discharge than is deposited on the 1st charge.[69] So there is some residual MnO_2 on the electrode after the 2nd discharge. This phenomenon continues during the early cycles. In other words, the dissolution of MnO_2 does not catch up with the deposition of MnO_2 during the early stage of cycling. So there is

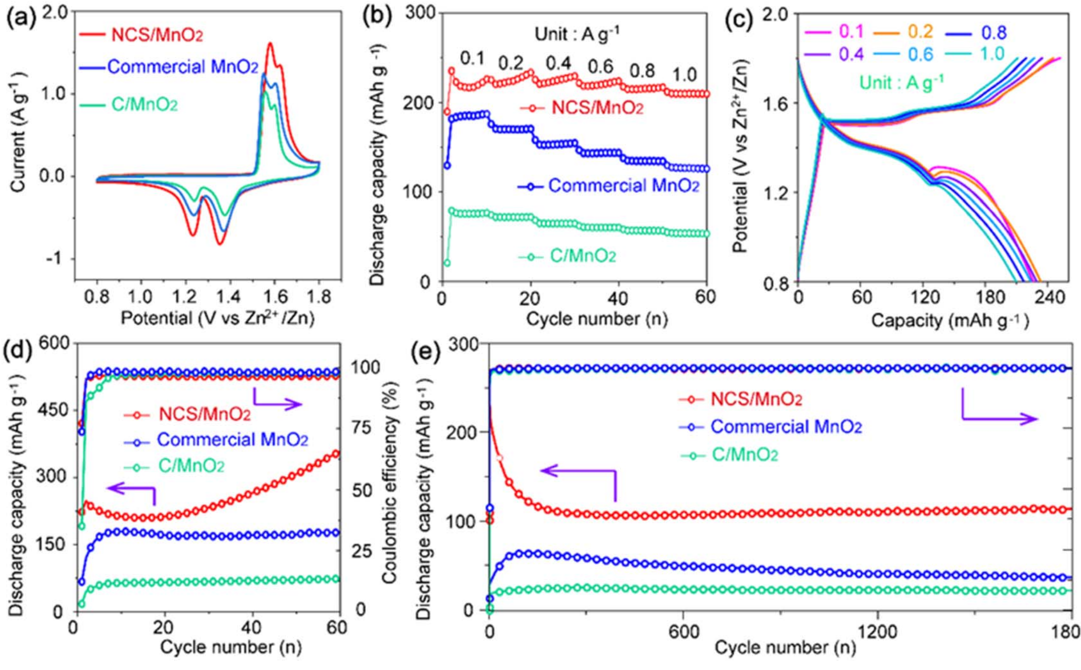

Fig. 3 Electrochemical behavior in ZIB cathodes: (a) CV curves at a scan rate of 0.2 mV s^{-1}. (b) Rate performance. (c) Galvanostatic discharge/charge profiles of NCS/MnO_2 at different current densities. (d) Cycling performance at 0.2 A g^{-1}. (e) Cycling performance at 2 A g^{-1}.

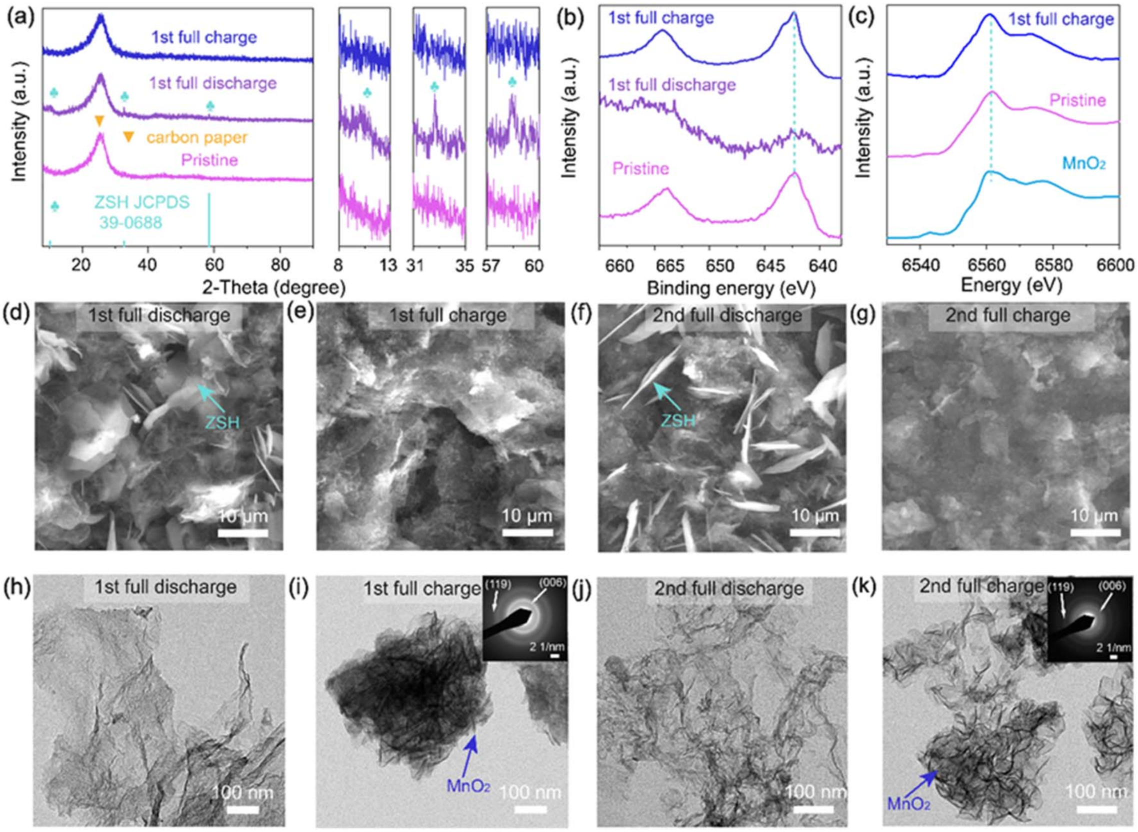

Fig. 4 Structural evolution of NCS/MnO_2 electrode during discharge/charge process: (a) XRD patterns; (b) XPS spectra Mn 2p; (c) XAS; (d–g) SEM images (h–k) TEM images.

more residual MnO_2 on the electrode with cycling, decreasing the conductivity of the electrode.[70] As a result, the capacity fades. As seen in Fig. 3e, the capacity of for NCS/MnO_2 still can be maintained at 114 mA h g^{-1} after 1800 cycles. For a comparison, low capacities are attained for C/MnO_2 (22 mA h g^{-1}) and commercial MnO_2 (37 mA h g^{-1}). The excellent performance of NCS/MnO_2 is also superior to most of reported Mn-based cathodes (Table S3†).

To further manifest the advantages of BC as carbon source, filter paper (FP) and printer paper (PP) were also immersed in urea solution following the same protocol as BC. The FTIR spectra of dried urea/filter paper and dried urea/printer paper are similar as their pristine ones and just display a few weak peaks coming from urea (Fig. S13†), implying that urea is also absorbed on these papers, but the amount is very small. Conversely, the FTIR spectra of dried urea/BC is completely consistent with urea. The mass of urea absorbed by filter paper and printer paper are respectively 0.004 and 0.005 g cm^{-2} (Table S4†), which is negligible in comparison with the BC case (0.15 g cm^{-2}). The mass ratio between absorbed urea and BC is 25, much higher than urea/FP (0.4) and urea/PP (0.6). These results clearly indicate the large BC water-absorbing capacity compared to regular microfibrous paper, allowing to incorporate large solute amounts that are retained and well distributed after drying. Given the small amount of added urea, there is no significant morphologic difference between MnO_2 derived from papers immersed or not immersed in urea, although a small capacity enhancement is still observed in treated samples (Fig. S14 and S15†).

Electrochemical impedance spectroscopy was conducted to further analyze the reaction kinetics of NCS/MnO_2, C/MnO_2 and commercial MnO_2 (Fig. S16†). The Nyquist plots is composed of one semicircle in the high frequency region and one straight line in the low frequency region. The semicircle is associated with charge-transfer resistance and the line is related to ion diffusion process.[71] NCS/MnO_2 shows a smaller semicircle than other C/MnO_2 and commercial MnO_2, revealing a smaller charge transfer resistance for NCS/MnO_2. The diffusion coefficient of these electrodes can be reflected by the Warburg coefficient σ, which is inversely proportional to the diffusion coefficient.[72] The σ values of these electrodes can be obtained by fitting the linear relation between Z' and $\omega^{-1/2}$. The σ values of NCS/MnO_2, C/MnO_2 and commercial MnO_2 are respectively 26, 50, and 77 Ω s^{-1}. The σ value of C/MnO_2 and commercial MnO_2 are nearly 2–3 times higher than NCS/MnO_2, showing the fast ion diffusion for NCS/MnO_2. The fast charge transfer and the ion diffusion of NCS/MnO_2 can be attributed to the optimal architecture of NCS. N-doping can enhance the electronic conductivity of carbon[73] and the high porosity can offer numerous channels for transporting ions.[74]

To better comprehend the electrochemical reaction mechanism of NCS/MnO_2, CV tests were conducted at different scan

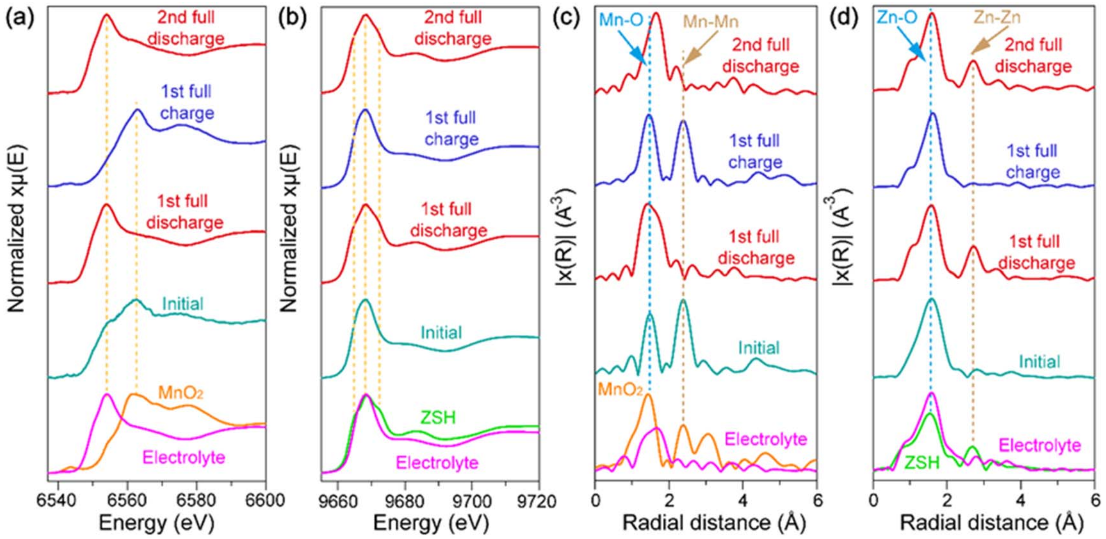

Fig. 5 *In situ* measurements of NCS/MnO_2 electrode: (a and b) Mn and Zn K-edge XANES spectra at selected states of charge and the Fourier transforms of their corresponding k^2-weighted EXAFS oscillations (c and d).

rates ranging from 0.2 to 1.0 mV s^{-1} (Fig. S17a†). The peaks slightly broaden without significant change of the CV. According to previous literature,[75] the charge storage kinetics can be expressed by the following equation: $i = a \cdot v^b$ (i: peak current; v: scan rate; a, b: variable values). The b value can be calculated by the slopes of the fitting curves of $\log i$ *versus* $\log v$ (Fig. S17b†). The b values of 1.0 and 0.5 respectively correspond to the capacitive-like behavior and the diffusion-controlled process.[76,77] The b value of these peaks are respectively 0.74, 0.79, 0.63 and 0.7 (Fig. S17c†), suggesting that the electrochemical reactions kinetics of NCS/MnO_2 contains both capacitive and diffusion-controlled processes. As the scan rate increases from 0.2 to 1.0 mV s^{-1}, the fraction of capacitive contribution gradually increases from 46 to 58% (Fig. S18†). This small variation with a 5-fold increase in scan rate confirms the good rate capability of our system.

Considering the capacity measured on the basis of the MnO_2 content as determined by TGA (Fig. S5†), we estimate up to 558 mA h $(g_{MnO_2})^{-1}$ at 0.2 A g^{-1} after 1st discharge. This value is considerably superior to the capacity expected for 1-electron reduction of MnO_2 (308 mA h $(g_{MnO_2})^{-1}$), and approaching the quantitative 2-electron reduction of MnO_2 to Mn^{2+} according to eqn (1):

$$MnO_2 + 4H^+ + 2e \rightleftharpoons Mn^{2+} + 2H_2O \tag{1}$$

However, such simple dissolution/precipitation mechanism is contradicted by the test reported above on the MnO_2-free carbons. The very small capacity they exhibited demonstrate that only a small amount of MnO_2 forms on charge from Mn^{2+} in solution, while samples with a substantial initial MnO_2 loading have much larger capacity. According to recent literature,[78] a key role is played by formation and dissolution zinc sulfate hydroxide hydrate ($Zn_4(OH)_6SO_4 \cdot 5H_2O$, ZSH) in parallel to MnO_2 dissolution and precipitation.

To confirm if this mechanism also applies to NCS/MnO_2, its structural evolution was followed during the process of discharge and charge. *Ex situ* SEM, TEM, XRD, XPS and XAS analyses were conducted during the initial 2 cycles of galvanostatic discharge/charge at 0.2 A g^{-1} (Fig. S19†). After the first full discharge, compared with the XRD pattern of pristine NCS/MnO_2 electrode, there are new peaks located at 32.6° and 58.5° (Fig. 4a and S20†), which are consistent with formation of ZSH.[79] SEM images show that large amounts of flakes emerge on the electrode of NCS/MnO_2 (Fig. 4e and S21b†) and these flakes can be assigned to ZSH.[80] TEM shows that the MnO_2 nanorods initially present in the NCS/MnO_2 cathode have vanished after the 1st full discharge (compare Fig. 4g and h). Consistently, only traces of Mn are still present on the surface, as indicated by XPS Mn 2p (Fig. 4b), demonstrating that MnO_2 actually dissolves during the discharge.[79] The generation of ZSH has been attributed to the dissolution reaction of MnO_2 into Mn^{2+}, which locally increases the pH, triggering the ZSH precipitation.[81,82] Upon the first full charge, these large ZSH flakes almost disappear (Fig. 4f and S21c†) and many new nanosheets show up. The energy of Mn XPS and XAS peaks almost return to that of the pristine state (Fig. 4b and c), further suggesting that re-deposition of MnO_2 occurs. To address the roles of ZSH and Mn^{2+} on the charge process, two NCS/MnO_2 cathodes (electrolyte: 2 M $ZnSO_4$ and 0.2 M $MnSO_4$) at the 1st full discharge were extracted from the cell. They were respectively removed of Mn^{2+} by washing, and of ZSH by acetic acid treatment (10 vol%). The Mn^{2+}-free cathode was assembled with 2 M $ZnSO_4$ electrolyte. The ZSH-free cathode (Fig. S22†) was assembled with the 2 M $ZnSO_4$ and 0.2 M $MnSO_4$ electrolyte. Then both cathodes were fully charged. The charge capacities of both electrodes are small and there are not obvious plateaus (Fig. S23†), suggesting that the occurrence of plateaus is indeed related to the simultaneous presence of both ZSH and Mn^{2+}. Images and XRD collected at the end of the second full discharge and charge suggest that the overall reactions are similar to those occurring during the 1st cycle (Fig. S24 and 25†).

The dissolution-precipitation mechanism is definitely confirmed by *in situ* Mn and Zn K-edge XAS spectra of NCS/MnO_2 electrode, reported in Fig. 5. Normalized Mn K-edge XANES spectra, exhibit a clear transfer from the component at 6561 eV that can be attributed to the Mn(IV) in the pristine MnO_2 to the one at 6553 eV after discharge, indicating the formation at its expense of reduced Mn^{2+} species. After charge the Mn environment is again very close to that found in the pristine electrode demonstrating the reversible Mn redox activity during the charge–discharge process. Unlike the Mn K-edge spectra, the Zn K-edge XANES spectra exhibit only small changes in the shape of the edge due to changes in the Zn local environment but they do not show any shift on the edge energy at all states of charge confirming that Zn ions are not redox active. Fig. 5c and d show the corresponding Fourier transform of the k^2 weighted Mn and Zn K-edge extended X-ray absorption fine structure (EXAFS) spectra, respectively. The strong peak located around 1.5 Å is attributed to the closest oxygen shell (Mn–O and Zn–O bond), while the peak around 2.5 Å is assigned to the metal–metal shell, absent in the case of solvated cations. At the fully discharged state the intensity of the Mn–Mn peak in suppressed, while the Mn-O distance slightly shifts to higher distances. This result confirms the formation of Mn^{2+} and reversible dissolution/precipitation of MnO_2 by discharging. Conversely, the Zn EXAFS is consistent with the reversible formation of a solid ZSH phase at the end of discharge without any redox activity. In light of this possible mechanism, we relate the long cycle life of the NCS/MnO_2 to its large area and high conductivity favoring optimal distribution of interfacial currents and dispersion of the precipitates.

Conclusions

In summary, we have reported the unexpected formation porous N-doped carbon nanosheet from carbonization of urea-impregnated BC. The optimal texture and electric properties of NCS are demonstrated in aqueous ZIBs. NCS is employed as a support for the growth of highly dispersed nanostructured MnO_2. The obtained NCS/MnO_2 processed as cathode provides a superior performance (114 mA h g^{-1} at 2 A g^{-1} after 1800 cycles) compared to commercial MnO_2 and many cathodes reported in literature. With advantages of highly porous and conductive carbon networks, NCS/MnO_2 exhibits remarkable capacity, excellent rate capability and long cycle life. Besides, the charge storage mechanism and the corresponding phase transformation of NCS/MnO_2 were evaluated by multiple characterization methods, supporting a MnO_2 2-electron full dissolution-deposition mechanism that appears highly reversible thanks to the unique properties of this bacterial cellulose derived composite. Considering the simple, green and scalable fabrication, NCS/MnO_2 can be a promising cathode candidate for high-performance ZIBs.

Conflicts of interest

The authors have no conflicts of interest to declare.

Acknowledgements

This research was funded by the Spanish Agency for Research (AEI) with ERDF cofunding, through the "Severo Ochoa" Programme for Centers of Excellence in R&D (FUNFUTURE, CEX2019-000917-S), the projects RTI2018-096273-B-I00, PID2021-124681OB-I00, and TED2021-132707B-I00. This research has been partially developed within the CSIC Interdisciplinary Thematic Platform (PTI+) Transición Energética Sostenible+ (PTI-TRANSENER+) as part of the CSIC program for the Spanish Recovery, Transformation and Resilience Plan funded by the Recovery and Resilience Facility of the European Union, established by the Regulation (EU) 2020/2094. W. W. and C. L. are grateful for the support from the China Scholarship Council (CSC No.: 201808340076 and 202106370079). This work has been performed within the framework of the doctoral program in materials science of UAB (W. W. and C. L.). XAS experiments were performed at CLAESS beamline of ALBA Synchrotron with the collaboration of ALBA staff.

References

1 N. Liu, X. Wu, Y. Yin, A. Chen, C. Zhao, Z. Guo, L. Fan and N. Zhang, *ACS Appl. Mater. Interfaces*, 2020, **12**, 28199–28205.
2 H. Jia, Z. Wang, B. Tawiah, Y. Wang, C.-Y. Chan, B. Fei and F. Pan, *Nano Energy*, 2020, **70**, 104523.
3 P. Ruan, X. Chen, L. Qin, Y. Tang, B. Lu, Z. Zeng, S. Liang and J. Zhou, *Adv. Mater.*, 2023, DOI: **10.1002/adma.202300577**.
4 Z. Yi, G. Chen, F. Hou, L. Wang and J. Liang, *Adv. Energy Mater.*, 2020, **11**, 2003065.
5 H. Zhang, X. Liu, H. Li, I. Hasa and S. Passerini, *Angew. Chem., Int. Ed.*, 2021, **60**, 598–616.
6 Y. Lv, Y. Xiao, L. Ma, C. Zhi and S. Chen, *Adv. Mater.*, 2022, **34**, 2106409.
7 N. Zhang, X. Chen, M. Yu, Z. Niu, F. Cheng and J. Chen, *Chem. Soc. Rev.*, 2020, **49**, 4203–4219.
8 J. Huang, Y. Li, R. Xie, J. Li, Z. Tian, G. Chai, Y. Zhang, F. Lai, G. He, C. Liu, T. Liu and D. J. L. Brett, *J. Energy Chem.*, 2021, **58**, 147–155.
9 L. E. Blanc, D. Kundu and L. F. Nazar, *Joule*, 2020, **4**, 771–799.
10 L. Godeffroy, I. Aguilar, J. Médard, D. Larcher, J. M. Tarascon and F. Kanoufi, *Adv. Energy Mater.*, 2022, **12**, 2200722.
11 X. Chen, P. Ruan, X. Wu, S. Liang and J. Zhou, *Acta Phys. -Chim. Sin.*, 2021, **38**, 2111003.
12 Y. Liu, X. Chi, Q. Han, Y. Du, J. Huang, Y. Liu and J. Yang, *J. Power Sources*, 2019, **443**, 227244.
13 Y. Zhao, Y. Zhu and X. Zhang, *InfoMat*, 2019, **2**, 237–260.
14 J. Huang, Z. Wang, M. Hou, X. Dong, Y. Liu, Y. Wang and Y. Xia, *Nat. Commun.*, 2018, **9**, 2906.
15 C. Wang, Y. Zeng, X. Xiao, S. Wu, G. Zhong, K. Xu, Z. Wei, W. Su and X. Lu, *J. Energy Chem.*, 2020, **43**, 182–187.
16 X. Shen, X. Wang, Y. Zhou, Y. Shi, L. Zhao, H. Jin, J. Di and Q. Li, *Adv. Funct. Mater.*, 2021, **31**, 2101579.

17 Y. Fu, Q. Wei, G. Zhang, X. Wang, J. Zhang, Y. Hu, D. Wang, L. Zuin, T. Zhou, Y. Wu and S. Sun, *Adv. Energy Mater.*, 2018, **8**, 1801445.

18 C. Hu, Y. Lin, J. W. Connell, H. M. Cheng, Y. Gogotsi, M. M. Titirici and L. Dai, *Adv. Mater.*, 2019, **31**, 1806128.

19 H. Yu, G. Liu, M. Wang, R. Ren, G. Shim, J. Y. Kim, M. X. Tran, D. Byun and J. K. Lee, *ACS Appl. Mater. Interfaces*, 2020, **12**, 5820–5830.

20 D. Hursan, A. A. Samu, L. Janovak, K. Artyushkova, T. Asset, P. Atanassov and C. Janaky, *Joule*, 2019, **3**, 1719–1733.

21 Z. Sheng, P. Qi, Y. Lu, G. Liu, M. Chen, X. Gan, Y. Qin, K. Hao and Y. Tang, *ACS Appl. Mater. Interfaces*, 2021, **13**, 34495–34506.

22 A. Samanta, B. K. Barman, S. Mallick and C. R. Raj, *ACS Appl. Energy Mater.*, 2020, **3**, 10108–10118.

23 B. He, Z. Zhou, P. Man, Q. Zhang, C. Li, L. Xie, X. Wang, Q. Li and Y. Yao, *J. Mater. Chem. A*, 2019, **7**, 12979–12986.

24 S. Wang, C. M. McGuirk, A. d'Aquino, J. A. Mason and C. A. Mirkin, *Adv. Mater.*, 2018, **30**, 1800202.

25 Z. Wang, J. Huang, J. Mao, Q. Guo, Z. Chen and Y. Lai, *J. Mater. Chem. A*, 2020, **8**, 2934–2961.

26 S. M. J. Rogge, M. Waroquier and V. Van Speybroeck, *Acc. Chem. Res.*, 2018, **51**, 138–148.

27 S. Roig-Sanchez, E. Jungstedt, I. Anton-Sales, D. C. Malaspina, J. Faraudo, L. A. Berglund, A. Laromaine and A. Roig, *Nanoscale Horiz.*, 2019, **4**, 634–641.

28 A. Alonso-Díaz, J. Floriach-Clark, J. Fuentes, M. Capellades, N. S. Coll and A. Laromaine, *ACS Biomater. Sci. Eng.*, 2019, **5**, 413–419.

29 M. Gao, J. Li, Z. Bao, M. Hu, R. Nian, D. Feng, D. An, X. Li, M. Xian and H. Zhang, *Nat. Commun.*, 2019, **10**, 437.

30 J. Caro-Astorga, K. T. Walker, N. Herrera, K. Y. Lee and T. Ellis, *Nat. Commun.*, 2021, **12**, 5027.

31 E. Tsouko, S. Maina, D. Ladakis, I. K. Kookos and A. Koutinas, *Renewable Energy*, 2020, **160**, 944–954.

32 C. Chen, W. Ding, H. Zhang, L. Zhang, Y. Huang, M. Fan, J. Yang and D. Sun, *Carbohydr. Polym.*, 2022, **278**, 118995.

33 J. Wang, J. Tavakoli and Y. Tang, *Carbohydr. Polym.*, 2019, **219**, 63–76.

34 L. Ma, Z. Bi, Y. Xue, W. Zhang, Q. Huang, L. Zhang and Y. Huang, *J. Mater. Chem. A*, 2020, **8**, 5812–5842.

35 J. Xu, J. Rong, F. Qiu, Y. Zhu, K. Mao, Y. Fang, D. Yang and T. Zhang, *J. Colloid Interface Sci.*, 2019, **555**, 294–303.

36 Y. Zhang, J. Tan, F. Wen, Z. Zhou, M. Zhu, S. Yin and H. Wang, *Int. J. Hydrogen Energy*, 2018, **43**, 6167–6176.

37 A. Dobashi, J. Maruyama, Y. Shen, M. Nandi and H. Uyama, *Carbohydr. Polym.*, 2018, **200**, 381–390.

38 Y. Gao, D. He, L. Wu, Z. Wang, Y. Yao, Z.-H. Huang, H. Yang and M.-X. Wang, *Chem. Eng. J.*, 2021, **420**, 127411.

39 W. Wang, S. Khabazian, S. Roig-Sanchez, A. Laromaine, A. Roig and D. Tonti, *Renewable Energy*, 2021, **177**, 209–215.

40 W. Wang, S. Khabazian, M. Casas-Papiol, S. Roig-Sanchez, A. Laromaine, A. Roig and D. Tonti, *Int. J. Hydrogen Energy*, 2022, **47**, 29753–29761.

41 L. Simonelli, C. Marini, W. Olszewski, M. Ávila Pérez, N. Ramanan, G. Guilera, V. Cuartero, K. Klementiev and N. L. Saini, *Cogent Phys.*, 2016, **3**, 1231987.

42 G. Wang, Y. Sun, D. Li, W. Wei, X. Feng and K. Mullen, *Small*, 2016, **12**, 3914–3919.

43 K. Zhang, H. Zhao, Z. Zhang, J. Chen, X. Mu, X. Pan, Z. Zhang, J. Zhou, J. Li and E. Xie, *Carbon*, 2015, **95**, 746–755.

44 Y. Zhang, Z. Wang, K. Hu, J. Ren, N. Yu, X. Liu, G. Wu and N. Liu, *Energy Storage Mater.*, 2021, **34**, 311–319.

45 P. P. Ghimire, M. Gao and M. Jaroniec, *Carbon*, 2019, **153**, 206–216.

46 J. Li, Y. Chen, J. Guo, F. Wang, H. Liu and Y. Li, *Adv. Funct. Mater.*, 2020, **30**, 2004115.

47 H. Wang, F. X. Yin, N. Liu, R. H. Kou, X. B. He, C. J. Sun, B. H. Chen, D. J. Liu and H. Q. Yin, *Adv. Funct. Mater.*, 2019, **29**, 1901531.

48 A. Singhania and A. N. Bhaskarwar, *Renewable Energy*, 2018, **127**, 509–513.

49 S. Li, Z. Lei, G. Yu, Q. Xu, W. Xu, R. Wu and M. K. Banks, *ACS Sustainable Chem. Eng.*, 2020, **8**, 12768–12774.

50 M. Yuan, F. Luo, Y. Rao, J. Yu, Z. Wang, H. Li and X. Chen, *Carbon*, 2021, **183**, 128–137.

51 K. Wang, Y. Chen, R. Tian, H. Li, Y. Zhou, H. Duan and H. Liu, *ACS Appl. Mater. Interfaces*, 2018, **10**, 11333–11342.

52 R. Wang, M. He, Y. Zhou, S. Nie, Y. Wang, W. Liu, Q. He, W. Wu, X. Bu and X. Yang, *Carbon*, 2020, **156**, 378–388.

53 Z. Weng, K. Zhang, Y. Qi, T. Zhang, M. Xia, F. Hu, S. Zhang, C. Liu, J. Wang and X. Jian, *Carbon*, 2020, **159**, 495–503.

54 A. Eftekhari and Z. Fan, *Mater. Chem. Front.*, 2017, **1**, 1001–1027.

55 A. R. Selvaraj, A. Muthusamy, C. Inho, H.-J. Kim, K. Senthil and K. Prabakar, *Carbon*, 2021, **174**, 463–474.

56 L. Jin, X. Guo, R. Gong, J. Zheng, Z. Xiang, C. Zhang and J. P. Zheng, *Energy Storage Mater.*, 2019, **23**, 409–417.

57 T. Le, Y. Yang, L. Yu, Z. H. Huang and F. Kang, *Sci. Rep.*, 2016, **6**, 37368.

58 A. E. Fischer, K. A. Pettigrew, D. R. Rolison, R. M. Stroud and J. W. Long, *Nano Lett.*, 2007, **7**, 281–286.

59 G. Li, J. Sun, W. Hou, S. Jiang, Y. Huang and J. Geng, *Nat. Commun.*, 2016, **7**, 10601.

60 J. Zhang, W. Zhu, Y. Pei, Y. Liu, Y. Qin, X. Zhang, Q. Wang, Y. Yin and M. D. Guiver, *ChemSusChem*, 2019, **12**, 4165–4169.

61 J. Wang, Z. Yang, Y. Li, X. Fan, F. Zhang, G. Zhang, W. Peng and S. Wang, *Carbon*, 2020, **163**, 43–55.

62 F. Zheng, Y. Yang and Q. Chen, *Nat. Commun.*, 2014, **5**, 5261.

63 H. Huang, R. Xu, Y. Feng, S. Zeng, Y. Jiang, H. Wang, W. Luo and Y. Yu, *Adv. Mater.*, 2020, **32**, 1904320.

64 E. S. Ilton, J. E. Post, P. J. Heaney, F. T. Ling and S. N. Kerisit, *Appl. Surf. Sci.*, 2016, **366**, 475–485.

65 Y. Zhao, P. Zhang, J. Liang, X. Xia, L. Ren, L. Song, W. Liu and X. Sun, *Energy Storage Mater.*, 2022, **47**, 424–433.

66 F. Tang, J. Gao, Q. Ruan, X. Wu, X. Wu, T. Zhang, Z. Liu, Y. Xiang, Z. He and X. Wu, *Electrochim. Acta*, 2020, **353**, 136570.

67 H. Moon, K. H. Ha, Y. Park, J. Lee, M. S. Kwon, J. Lim, M. H. Lee, D. H. Kim, J. H. Choi, J. H. Choi and K. T. Lee, *Adv. Sci.*, 2021, **8**, 2003714.

68 H. Pan, Y. Shao, P. Yan, Y. Cheng, K. S. Han, Z. Nie, C. Wang, J. Yang, X. Li, P. Bhattacharya, K. T. Mueller and J. Liu, *Nat. Energy*, 2016, **1**, 16039.

69 D. Wu, L. M. Housel, S. J. Kim, N. Sadique, C. D. Quilty, L. Wu, R. Tappero, S. L. Nicholas, S. Ehrlich, Y. Zhu, A. C. Marschilok, E. S. Takeuchi, D. C. Bock and K. J. Takeuchi, *Energy Environ. Sci.*, 2020, **13**, 4322–4333.

70 Y. Zhou, X. Cheng, B. Tynan, Z. Sha, F. Huang, M. S. Islam, J. Zhang, A. N. Rider, L. Dai, D. Chu, D.-W. Wang, Z. Han and C.-H. Wang, *Carbon*, 2021, **184**, 504–513.

71 R. Liang, J. Fu, Y.-P. Deng, Y. Pei, M. Zhang, A. Yu and Z. Chen, *Energy Storage Mater.*, 2021, **36**, 478–484.

72 B. Sambandam, S. Kim, D. T. Pham, V. Mathew, J. Lee, S. Lee, V. Soundharrajan, S. Kim, M. H. Alfaruqi, J.-Y. Hwang and J. Kim, *Energy Storage Mater.*, 2021, **35**, 47–61.

73 H. He, D. Huang, Y. Tang, Q. Wang, X. Ji, H. Wang and Z. Guo, *Nano Energy*, 2019, **57**, 728–736.

74 M. Yang, Y. Wang, Z. Sun, H. Mi, S. Sun, D. Ma and P. Zhang, *J. Energy Chem.*, 2022, **67**, 645–654.

75 J. Wang, J. G. Wang, X. Qin, Y. Wang, Z. You, H. Liu and M. Shao, *ACS Appl. Mater. Interfaces*, 2020, **12**, 34949–34958.

76 D. Chao, C. R. Zhu, M. Song, P. Liang, X. Zhang, N. H. Tiep, H. Zhao, J. Wang, R. Wang, H. Zhang and H. J. Fan, *Adv. Mater.*, 2018, **30**, 1803181.

77 G. Fang, C. Zhu, M. Chen, J. Zhou, B. Tang, X. Cao, X. Zheng, A. Pan and S. Liang, *Adv. Funct. Mater.*, 2019, **29**, 1808375.

78 C. Li, X. Chi, J. Huang, J. Wu and Y. Liu, *ACS Appl. Energy Mater.*, 2022, **5**, 1478–1486.

79 X. Zeng, J. Liu, J. Mao, J. Hao, Z. Wang, S. Zhou, C. D. Ling and Z. Guo, *Adv. Energy Mater.*, 2020, **10**, 1904163.

80 J. Zhou, M. Xie, F. Wu, Y. Mei, Y. Hao, L. Li and R. Chen, *Adv. Mater.*, 2022, **34**, 2106897.

81 X. Xie, H. Fu, Y. Fang, B. Lu, J. Zhou and S. Liang, *Adv. Energy Mater.*, 2022, **12**, 2102393.

82 X. Guo, J. Zhou, C. Bai, X. Li, G. Fang and S. Liang, *Mater. Today Energy*, 2020, **16**, 100396.